Research Article | Vol. 26, No. 7 | 2 Apr 2018 | OPTICS EXPRESS 8059
Optics EXPRESS

12.5 Gbit/s discretely tunable InP-on-silicon filtered feedback laser with sub-nanosecond wavelength switching times

SÖREN DHOORE,[1,2,*] ABDUL RAHIM,[1,2] GUNTHER ROELKENS,[1,2] AND GEERT MORTHIER [1,2]

[1] *Photonics Research Group, INTEC, Ghent University-IMEC, B-9052, Ghent, Belgium*
[2] *Center for Nano-and Biophotonics (NB-Photonics), Ghent University, B-9052, Ghent, Belgium*
[*] *Soren.Dhoore@UGent.be*

Abstract: A heterogeneously integrated InP-on-silicon fast tunable filtered feedback laser is demonstrated. The laser device consists of a main Fabry-Pérot cavity connected to an integrated arrayed waveguide grating of which the outputs form external cavities in which semiconductor optical amplifiers can be switched to provide single-mode operation and tunability. The laser can operate at four different wavelengths whereby switching between each wavelength channel is done within one nanosecond. For each wavelength channel 12.5 Gbit/s NRZ-OOK direct modulation is demonstrated. The combination of fast wavelength switching with straightforward wavelength control and high-speed direct modulation characteristics make the demonstrated laser structure very attractive for use in optical packet or burst switching systems.

OCIS codes: (140.3600) Lasers, tunable, (230.7408) Wavelength filtering devices, (250.5300) Photonic integrated circuits.

References and links

1. M. A. Mestre, J. M. Estarán, P. Jennevé, H. Mardoyan, I. T. Monroy, D. Zibar, and S. Bigo, "Novel coherent optical OFDM-based transponder for optical slot switched networks," J. Lightw. Technol. **34**(8), 1851–1858 (2016).
2. D. Cotter, R. J. Manning, K. J. Blow, A. D. Ellis, A. E. Kelly, D. Nesset, I. D. Phillips, A. J. Poustie, and D. C. Rogers, "Nonlinear optics for high-speed digital information processing," Science **286**(5444), 1523–1528 (1999).
3. D. J. Blumenthal, J. E. Bowers, L. Rau, H.-F. Chou, S. Rangarajan, W. Wang, and K. N. Poulsen, "Optical signal processing for optical packet switching networks," IEEE Commun. Mag. **41**(2), 23–29 (2003).
4. M. A. Ettabib, C. Lacava, Z. Liu, A. Bogris, A. Kapsalis, M. Brun, P. Labeye, S. Nicoletti, D. Syvridis, D. J. Richardson, and P. Petropoulos, "Wavelength conversion of complex modulation formats in a compact SiGe waveguide," Opt. Express **25**(4), 3252–3258 (2017).
5. Q. Huang, Y.-K. Yeo, and L. Zhou, "A single-stage optical load-balanced switch for data centers," Opt. Express **20**(22), 25014–25021 (2012).
6. C.-K. Chan, K. L. Sherman, and M. Zirngibl, "A fast 100-channel wavelength-tunable transmitter for optical packet switching," IEEE Photon. Technol. Lett. **13**(7), 729–731 (2001).
7. Y. When, H. Jin, M. Chen, and V. C. M. Leung, "Enabling technologies for future data center networking: a primer," IEEE Network. **27**(4), 8–15 (2013).
8. S. Srinivasan, A. Y. Liu, D. Liang, and J. E. Bowers, "Silicon lasers and photonic integrated circuits," in *Fibre Optic Communication* (Springer, 2017), pp. 739–797.
9. G. Roelkens, A. Abbasi, P. Cardile, U. Dave, A. De Groote, Y. De Koninck, S. Dhoore, X. Fu, A. Gassenq, N. Hattasan, Q. Huang, S. Kumari, S. Keyvaninia, B. Kuyken, L. Li, P. Mechet, M. Muneeb, D. Sanchez, H. Shao, T. Spuesens, A. Z. Subramanian, S. Uvin, M. Tassaert, K. Van Gasse, J. Verbist, R. Wang, Z. Wang, J. Zhang, J. Van Campenhout, X. Yin, J. Bauwelinck, G. Morthier, R. Baets, and D. Van Thourhout, "III-V-on-silicon photonic devices for optical communication and sensing," Photonics **2**(3), 969–1004 (2015).
10. S. Dhoore, G. Roelkens, and G. Morthier, "III-V-on-silicon three-section DBR laser with over 12 nm continuous tuning range," Opt. Lett. **42**(6), 1121–1124 (2017).
11. S. Dhoore, L. Li, A. Abbasi, G. Roelkens, and G. Morthier, "Demonstration of a discretely tunable III-V-on-silicon sampled grating DFB laser," IEEE Photon. Technol. Lett. **28**(21), 2343–2346 (2016).
12. G. Kurczveil, J. M. Heck, J. D. Peters, J. M. Garcia, D. Spencer, and J. E. Bowers, "An integrated hybrid silicon multiwavelength AWG laser," IEEE J. Sel. Topics Quantum Electron. **17**(6), 1521–1527 (2011).
13. S. Keyvaninia, S. Verstuyft, S. Pathak, F. Lelarge, G.-H. Duan, D. Bordel, J.-M. Fedeli, T. De Vries, B. Smalbrugge, E. J. Geluk, J. Bolk, M. Smit, G. Roelkens, and D. Van Thourhout, "III-V-on-silicon multi-frequency lasers,"

#322517 https://doi.org/10.1364/OE.26.008059
Journal © 2018 Received 13 Feb 2018; revised 14 Mar 2018; accepted 14 Mar 2018; published 20 Mar 2018

Optics EXPRESS

Opt. Express **21**(11), 13675–13683 (2013).
14. B. Docter, J. Pozo, S. Beri, I. V. Ermakov, J. Danckaert, M. K. Smit, and F. Karouta, "Discretely tunable laser based on filtered feedback for telecommunication applications," IEEE J. Sel. Topics Quantum Electron. **16**(5), 1405–1412 (2010).
15. D. M. Kane, and K. A. Shore, *Unlocking dynamical diversity: optical feedback effects on semiconductor lasers* (Wiley, 2005).
16. H. Erzgräber, and B. Krauskopf, "Dynamics of a filtered-feedback laser: influence of the filter width," Opt. Lett. **32**(16), 2441–2443 (2007).
17. S. Keyvaninia, S. Verstuyft, L. Van Landschoot, F. Lelarge, G.-H. Duan, S. Messaoudene, J.-M. Fedeli, T. De Vries, B. Smalbrugge, E. J. Geluk, J. Bolk, M. Smit, G. Morthier, D. Van Thourhout, and G. Roelkens, "Heterogeneously integrated III-V/silicon distributed feedback lasers," Opt. Lett. **38**(24), 5434–5437 (2013).
18. W. Bogaerts, S.K. Selvaraja, P. Dumon, J. Brouckaert, K. De Vos, D. Van Thourhout, and R. Baets, "Silicon-on-insulator spectral filters fabricated with CMOS technology," IEEE J. Sel. Topics Quantum Electron. **16**(1), 33–44 (2010).
19. L. A. Coldren, S. W. Corzine, and M. L. Mašanović, *Diode Lasers and Photonic Integrated Circuits* (Wiley, 2012).
20. D. Vermeulen, Y. De Koninck, Y. Li, E. Lambert, W. Bogaerts, R. Baets, and G. Roelkens, "Reflectionless grating couplers for Silicon-on-Insulator photonic integrated circuits," Opt. Express **20**(20), 22278–22283 (2012).
21. B. Docter, J. Pozo, I. V. Ermakov, X. J. M. Leijtens, F. Karouta, S. Beri, J. Danckaert, and M. K. Smit, "Integrated filtered-feedback tunable laser with enhanced control of feedback phase," in Proceedings of Symposium IEEE Photonics Benelux Chapter (IEEE, 2010), pp. 285–288.
22. J. Cho, C. Xie, and P. J. Winzer, "Analysis of soft-decision FEC on non-AWGN channels," Opt. Express **20**(7), 7915–7928 (2012).
23. G. Morthier, R. Schatz, and O. Kjebon, "Extended modulation bandwidth of DBR and external cavity lasers by utilizing a cavity resonance for equalization," IEEE J. Quantum Electron. **36**(12), 1468–1475 (2000).
24. A. Abbasi, B. Moeneclaey, J. Verbist, X. Yin, J. Bauwelinck, G.-H. Duan, G. Roelkens, and G. Morthier, "Direct and electroabsorption modulation of a III-V-on-silicon DFB laser at 56 Gb/s," IEEE J. Sel. Topics Quantum Electron. **23**(6), 1–7 (2017).

1. Introduction

Datacenter networks based on optical packet or burst switching are expected to become a reality in the near future [1]. Envisioned implementations of such network architectures can make use of integrated nonlinear optical devices [2–4] but are typically based on passive wavelength routing devices and fast tunable lasers with tuning speeds on the order of several nanoseconds [5, 6]. Such tuning speeds are required as an optical packet has a typical length of a few hundred nanoseconds [7].

Over the past decades considerable effort has been put in the industrialization of silicon photonic devices. As efficient light emission is not possible from silicon itself, research has been directed towards the development of InP-on-silicon light sources for optical data- and telecommunication applications at 1310 nm and 1550 nm [8, 9]. Heterogeneously integrated InP-on-silicon lasers enable co-integration with passive silicon waveguide circuits, germanium photodetectors and high-speed silicon and germanium modulators.

So far nanosecond fast wavelength tuning with high-speed direct modulation characteristics has not been demonstrated with heterogeneously integrated InP-on-silicon lasers. Recently, we have experimentally demonstrated over 12 nm continuous wavelength tunability through current injection into the passive tuning layer of a tunable twin-guide (TTG) membrane of an InP-on-silicon distributed Bragg reflector (DBR) laser structure [10]. Tuning was, however, mainly thermal (and thus slow) because of the limited confinement factor of the optical mode in the tuning layer and because of the device's large thermal resistance. In earlier work, we achieved current-injection-based discrete thermal wavelength tuning over a 55 nm tuning range with an InP-on-silicon sampled grating distributed feedback (SG-DFB) laser [11].

In this paper, we demonstrate for the first time sub-nanosecond fast wavelength switching with an arrayed waveguide grating (AWG-)based InP-on-silicon laser structure that uses the filtered feedback principle to achieve single-mode laser operation and tunability. InP-on-silicon lasers making use of AWGs have been demonstrated before, where the AWG was an integral part of the laser cavity [12, 13]. Because of their long cavity length, such lasers usually have a

Optics EXPRESS

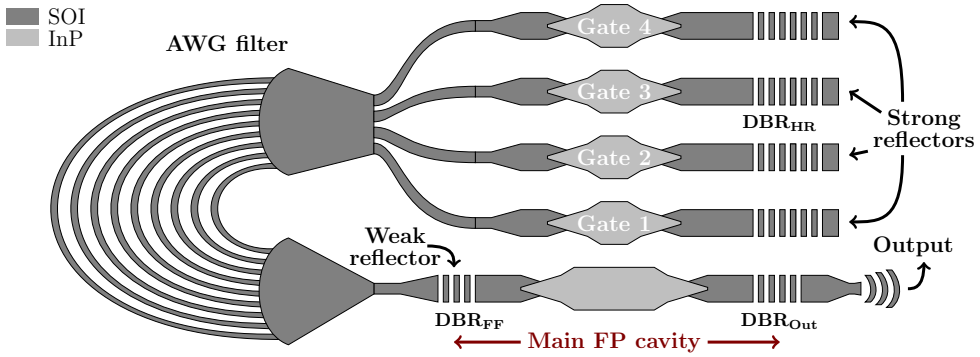

Fig. 1. Schematic of the demonstrated laser structure.

low modulation bandwidth. In our implementation the AWG is not part of the main cavity. The filtered feedback concept was first introduced and experimentally demonstrated by B. Docter et al. [14], where discrete wavelength tuning was achieved with a pure InP-based laser. The implementation on silicon, however, allows to benefit from the superior passive functionality of silicon, leading to improved static and dynamic lasing characteristics. This is also supported by our experimental results.

2. Laser design and fabrication

The laser structure is schematically shown in Fig. 1. The laser consists of a main Fabry-Pérot (FP) cavity with two partially reflective broadband silicon-on-insulator (SOI) DBR mirrors (denoted as DBR_{FF} and DBR_{Out} respectively, see section 2.3). At one side of the FP cavity the light output is coupled to an SOI arrayed waveguide grating (AWG) filter that demultiplexes the light in four different waveguide branches. In each branch an InP-on-silicon semiconductor optical amplifier (SOA) is implemented that can function as optical gate. If the SOA is biased at or above transparency, input light can be efficiently transmitted or even be amplified. When unbiased, all incident light is absorbed in the gate. By making use of a highly reflective SOI DBR mirror at the end of each waveguide branch (denoted as DBR_{HR}), light can be fed back to the laser. This enables the laser to operate in single-mode regime, close to the wavelength with maximum transmission through the AWG filter [15, 16]. Light exiting at the DBR_{Out} side is coupled towards a fiber-to-chip grating coupler for characterization of the laser device.

2.1. Semiconductor optical amplifier design

The SOAs that constitute the main FP cavity and the optical gates are implemented as InP-based *p-i-n* structures on top of SOI waveguides. The InP/InGaAsP layer stack consists of a 200 nm thick *p*-InGaAs top contact layer, a 1500 nm thick *p*-InP cladding layer, six 6 nm thick InGaAsP quantum wells (bandgap wavelength 1550 nm) surrounded by two 100 nm thick SCH InGaAsP layers (bandgap wavelength 1170 nm) and a 200 nm thick *n*-InP bottom contact layer. A 180 μm long double taper structure [17] is used to couple light from the SOA to the underlying silicon waveguide. For an InP taper tip width of 400 nm the simulated transition loss is 0.5 dB. The straight section of the main FP cavity and the gates is kept sufficiently short (240 μm and 40 μm respectively) to maximize the longitudinal mode spacing and minimize the transparency current respectively.

Optics EXPRESS

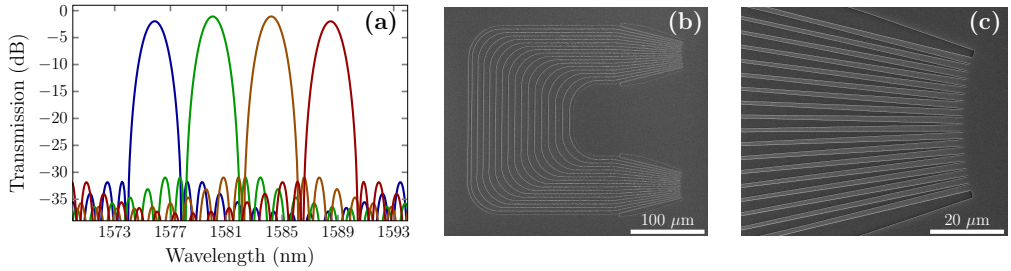

Fig. 2. AWG design. (a) Simulation of the AWG filter transmission; (b) SEM image of the AWG; (c) SEM image of the AWG (zoom on the star coupler region).

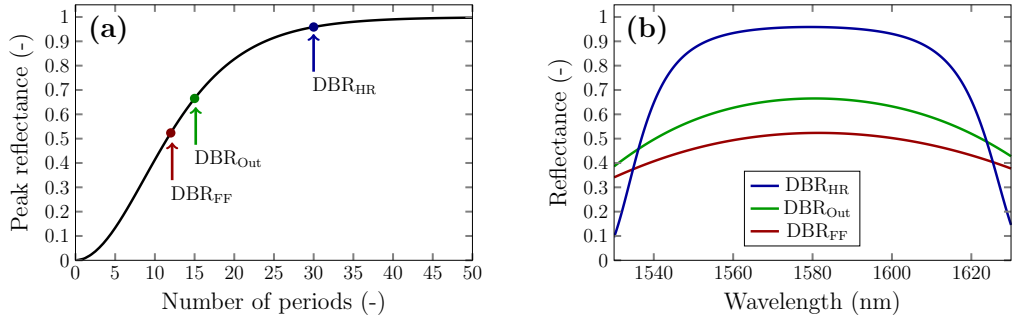

Fig. 3. DBR design. (a) Peak reflectance as a function of number of grating periods (Λ = 252 nm, duty cycle = 50%); (b) Reflection spectra for DBR_{FF}, DBR_{Out} and DBR_{HR}.

2.2. *Arrayed waveguide grating design*

The design of the AWG is done by means of the spectral toolbox from Luceda Photonics and follows the approach outlined in [18]. The AWG is acyclic and has $N = 4$ output channels with a designed channel spacing $\Delta\lambda_{AWG} = 4$ nm and free spectral range $FSR = \Delta\lambda_{AWG}(N + 1) = 20$ nm. The free space propagation region of both star couplers has a length of 71.6 μm, whereas the input and output aperture width is 1.8 μm. At the grating side the apertures are spaced 230 nm apart and 90 μm long linear tapers are used to connect the star coupler apertures with the grating arms. At the input and output side of the AWG the star coupler apertures are connected to the 650 nm wide rib waveguides using 45 μm long linear tapers. The simulated transmission characteristic for the different channels of the AWG is shown in Fig. 2(a). The 3 dB bandwidth of the passband of each wavelength channel is 1.2 nm. The AWG is implemented on an SOI wafer with a 400 nm thick device layer using a 180 nm etch. The shallow etch depth leads to reduced phase errors. SEM images of the fabricated AWG structure are shown in Fig. 2(b) and 2(c). The measured insertion loss of the AWG (characterized after complete device processing) is 4 dB.

2.3. *Distributed Bragg reflector design*

Three distinct DBR grating designs are used in the overall laser structure. One functions as semi-reflective output DBR grating (DBR_{Out}), one as low-reflective filtered feedback DBR grating (DBR_{FF}) and four as high-reflective DBR gratings (DBR_{HR}). In all three designs the DBRs have a silicon waveguide width of 2 μm and are implemented in a 400 nm thick device layer with 180 nm etch depth. The grating period is 252 nm in all DBR designs, which corresponds to a Bragg wavelength of 1580 nm, close to the gain peak wavelength of the InP stack. The reflectivity of the DBRs is determined by the number of grating periods, as shown in Fig. 3(a). The corresponding

Optics EXPRESS

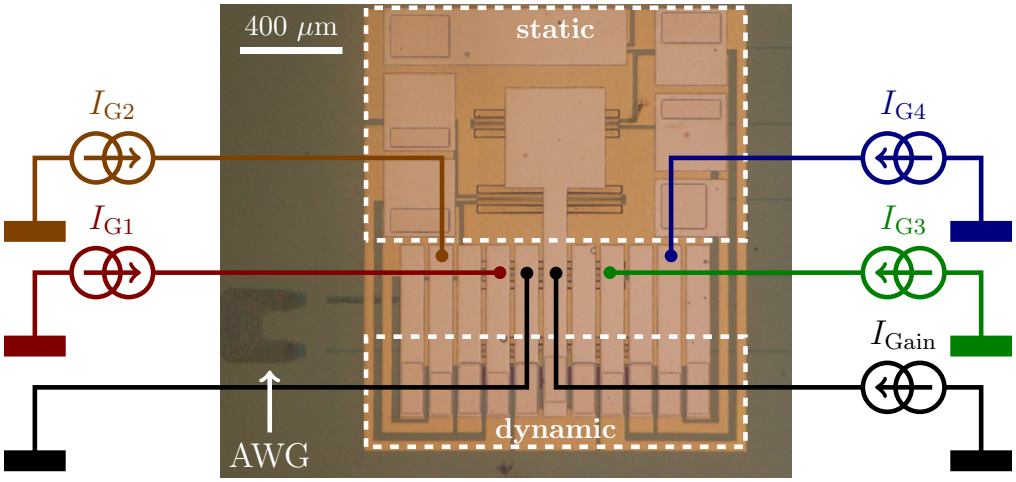

Fig. 4. Optical microscope image of the fabricated device. Naming of the different currents and contact pads for characterization are indicated. The upper contact pads are used for static characterization whereas the lower contact pads are used for dynamic characterization.

reflection spectra for the different DBR designs are shown in Fig. 3(b). The reflectivity of DBR_{HR} is larger than 95% whereas DBR_{Out} has a designed reflectivity of 66%, as trade-off between a low threshold current and large output power. The reflectivity of DBR_{FF} controls the filtered feedback strength γ (1/ns), which can phenomenologically be described as [14]

$$\gamma = \frac{1 - R_{DBR_{FF}}}{\tau_{in}} \sqrt{\frac{R_{DBR_{HR}}}{R_{DBR_{FF}}}} \left(1 - A_{DBR_{FF}}\right)^2 T_{AWG}^2 A_{Gate}^2, \tag{1}$$

where τ_{in} is the roundtrip time of the main FP cavity, $R_{DBR_{FF}}$ the reflectivity of DBR_{FF}, $R_{DBR_{HR}}$ the reflectivity of DBR_{HR}, T_{AWG} the transmission of the AWG and A_{Gate} the amplification of an SOA gate. $A_{DBR_{FF}}$ is given by $1 - T_{DBR_{FF}}/(1 - R_{DBR_{FF}})$ and accounts for scattering losses in DBR_{FF}, whereby it is assumed that $R_{DBR_{FF}} + T_{DBR_{FF}} < 1$. Generally, a small $R_{DBR_{FF}}$ leads to a larger γ but increased threshold current and vice versa. In our case $\tau_{in} = 2L_{FP}n_g/c = 16$ ps, with $L_{FP} = 600$ μm the total length of the main FP cavity (i.e. the distance between DBR_{FF} and DBR_{Out}), $n_g \approx 4.1$ the group index of the waveguide mode and c the speed of light. Assuming the gates are pumped to transparency ($A_{Gate} = 1$), $\gamma = 11$ ns^{-1} is obtained. With the feedback field being in phase with the propagating field, such filtered feedback strength can enable sub-ns wavelength switching times [14].

2.4. Fabrication

The SOI structures have a 400 nm thick silicon device layer with a single shallow etch depth of 180 nm and are fabricated in-house by means of electron-beam lithography (EBL) and subsequent reactive ion etching (RIE). The InP-on-silicon integration is based on adhesive divinylsiloxane-bis-benzocyclobutene (DVS-BCB) bonding. Ti/Au *p*-contact and Ni/Ge/Au *n*-contact metallurgies are used for all SOAs. Details of the bonding procedure and InP post processing can for instance be found in [9]. An optical microscope image of the fabricated device with indication of the different metal contact pads is shown in Fig. 4.

Optics EXPRESS

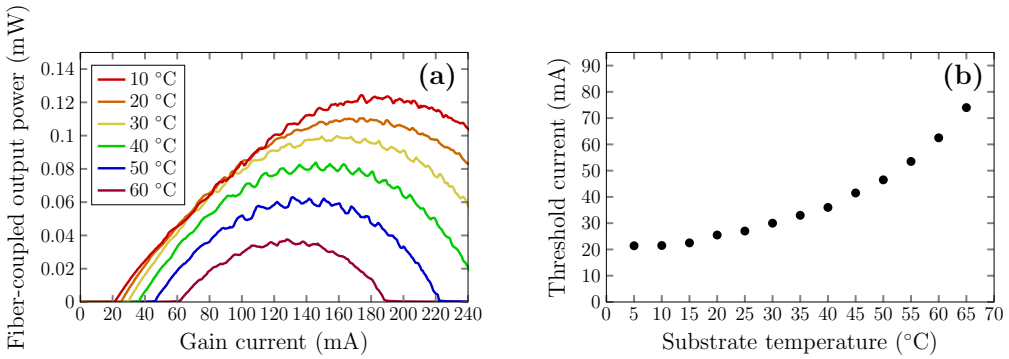

Fig. 5. Static laser characteristics. (a) LI curves at different substrate temperatures; (b) Dependence of the threshold current on the substrate temperature.

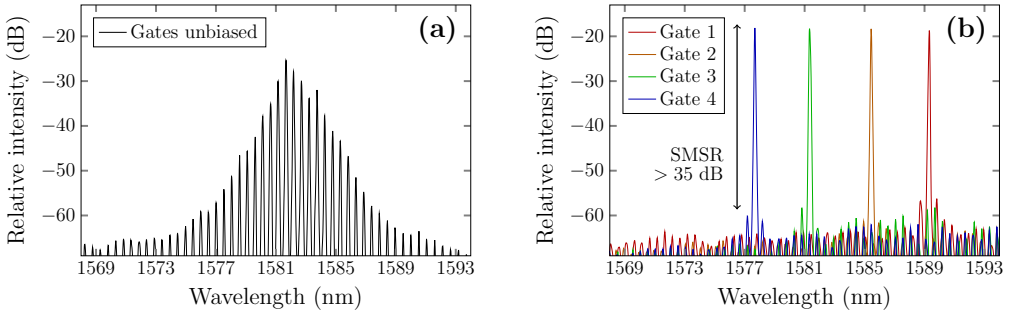

Fig. 6. Lasing spectra. (a) Gates are left unbiased; (b) Gates are biased above transparency.

3. Static laser characteristics

The laser device is characterized on a temperature-controlled stage. The direct current (DC) electrical characteristics are measured with two Keithley 2400 current sources and three electrical DC probes. The gain current and different gate currents are indicated as I_{Gain} and $I_{\mathrm{G}i}$, with $i = 1, \ldots 4$, respectively. The differential series resistances ($\mathrm{d}V/\mathrm{d}I$) in the main FP cavity and the optical gates are 3 Ω and 5 Ω, respectively. The optical properties are measured by coupling the ouput light from the chip to a standard single-mode optical fiber (SMF) by means of a reflectionless SOI grating coupler [20] at the $\mathrm{DBR}_{\mathrm{Out}}$ side. An HP 8153A power meter is used to measure the fiber-coupled optical output power. Figure 5(a) shows the light-current (LI) characteristics for the laser at different temperatures when the gates are left unbiased. Continuous-wave (CW) laser operation up to 65°C is achieved. At room temperature the laser threshold is 20 mA, with a maximum fiber-coupled output power of 0.1 mW. The grating coupler efficiency at the lasing wavelength is −16 dB (measured by means of a reference structure neighboring the laser device), which yields a maximum waveguide-coupled ouput power of 4 mW. The influence of the stage temperature on the lasing threshold is shown in Fig. 5(b).

Lasing spectra are measured with an Anritsu MS9740A optical spectrum analyzer (OSA). The lasing spectrum at room temperature for $I_{\mathrm{Gain}} = 80$ mA with unbiased gates is shown in Fig. 6(a). The lack of wavelength selectivity results in a typical Fabry-Pérot spectrum. The total length of the main FP cavity (L_{FP}) is 600 μm, which corresponds to a longitudinal mode spacing

Optics EXPRESS

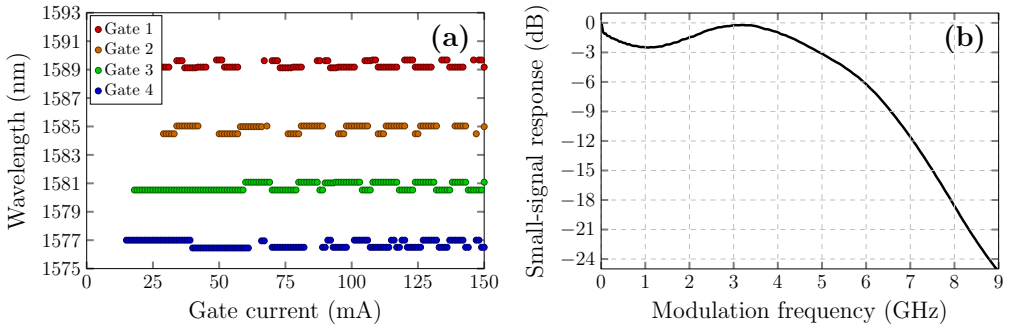

Fig. 7. (a) Influence of the gate current on the lasing wavelength (only data points with a SMSR > 35 dB are shown); (b) Small-signal modulation response for I_{Gain} = 80 mA and I_{G1} = 28 mA.

$\Delta\lambda_{\mathrm{FP}}$ = 0.5 nm, calculated from [19]

$$\Delta\lambda_{\mathrm{FP}} = \frac{\lambda^2}{2n_g L_{\mathrm{FP}}}, \tag{2}$$

with λ = 1580 nm the center wavelength. The same longitudinal mode spacing is also obtained from the measured optical spectrum. When one of the SOA gates is biased at or above transparency single-mode laser operation can be achieved because of the filtered feedback, as explained in section 2. Figure 6(b) shows the lasing spectra when the gates are appropriately biased. The transparency current varies between 20 mA and 24 mA for the different gates. Single-mode laser operation is achieved with a SMSR larger than 35 dB for all four wavelength channels. The channel spacing is 4 nm.

Figure 7(a) shows the peak lasing wavelength versus gate current for the different gates. At low gate currents (below transparency), the laser is not single-mode and operates at random wavelengths. Above transparency the laser can operate in single-mode regime. Generally the SMSR is larger than 35 dB. However, for certain gate currents the filtered optical feedback is out of phase with the oscillating laser mode, which effectively impedes single-mode operation. A large gate current leads to a large A_{Gate}, which leads to a large γ and which results in a larger SMSR at large gate currents as compared to lower gate currents. The 0.5 nm spaced mode hops are the result of a change in feedback phase and hence a different longitudinal mode selection, when the gate current is changed. In order to provide enhanced control of the feedback phase independently of the filtered feedback strength in future devices, a common phase control section could be added between the main FP cavity and the AWG input [21].

4. Dynamic laser characteristics

The dynamic characterization results include the small-signal laser characteristics, large-signal laser characteristics and the wavelength switching behavior between the different wavelength channels of the laser device.

4.1. Small-signal characteristics

Small-signal characterization of the laser is done using a Keysight PNA-X N5247A Microwave Network Analyzer. A small-amplitude radio frequency (RF) signal is combined with a DC I_{Gain} bias using a bias-tee. Using a 100 μm pitch high-speed GSG electrical probe the combined signal is connected to the amplifier of the main Fabry-Pérot cavity. One of the gate currents is appropriately biased to achieve single-mode laser operation. The small-signal response is shown

Optics EXPRESS

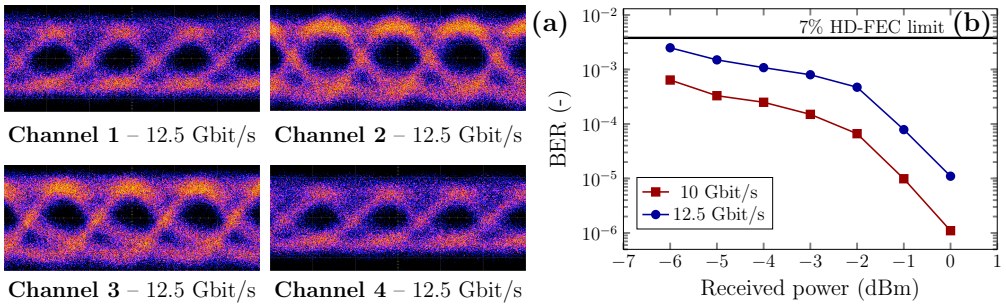

Fig. 8. Large-signal characteristics. (a) Eye diagrams for all four different wavelength channels under 12.5 Gbit/s direct modulation (back-to-back); (b) Bit error rate versus received power under 10 Gbit/s and 12.5 Gbit/s direct modulation (back-to-back).

in Fig. 7(b) for $I_{\text{Gain}} = 80$ mA and $I_{\text{G1}} = 28$ mA. A 6 dB bandwidth of 6 GHz is obtained. Similar bandwidths are found when the other wavelength channels are operated.

4.2. *Large-signal characteristics*

For the large-signal characterization of the laser a similar setup as for the small-signal characterization is used. This time a large-amplitude non-return-to-zero on-off-keying (NRZ-OOK) electrical signal is generated by means of a Keysight M8195A arbitrary waveform generator (AWG) at different bitrates. A 3 Vpp RF voltage swing is applied to the laser device with an $I_{\text{Gain}} = 80$ mA DC bias. Eye diagrams are measured by means of a 40 GHz Discovery Semiconductors *p-i-n* photodiode of which the output is connected to a Keysight DSA-Z63 real-time oscilloscope. Open eye diagrams are obtained up to 12.5 Gbit/s for the four different wavelength channels. This is shown in Fig. 8(a). Data streams are stored using the real-time oscilloscope and an off-line bit error rate (BER) analysis is performed. The recorded BER versus received optical power is shown in Fig. 8(b) for back-to-back operation at both 10 Gbit/s and 12.5 Gbit/s for a pseudo-random bit sequence (PRBS) with a word length of $2^7 - 1$. Clearly a BER below $3.8 \cdot 10^{-3}$ can be obtained, which enables error-free operation assuming 7% overhead hard decision forward error correction (HD-FEC) [22]. At a BER of 10^{-5} the power penalty for increasing the bitrate from 10 Gbit/s to 12.5 Gbit/s is 1 dB. At a BER of $5 \cdot 10^{-4}$ the power penalty is 3.3 dB, which is significantly larger as modulation is performed at the edge of the device bandwidth. We denote that a further increase of the direct modulation speed can be expected by exploiting the photon-photon resonance effect in the external cavities [23] and by making use of an optimized design with electrically isolated InP-to-silicon taper structures [24].

4.3. *Wavelength switching characteristics*

The measurement setup for characterization of the wavelength switching behavior is shown in Fig. 9. An Anritsu MP2100A pulse-pattern generator (PPG) and a 100 μm pitch high-speed GSGSG electrical probe are used to differentially drive the bias in two neighboring gates while I_{Gain} remains fixed. The light output from the laser device is then amplified by an Erbium-Doped Fiber Amplifier (EDFA) and sent through a Santec OTF-350 tunable bandpass filter. The latter allows to filter out one of the wavelength channels upon switching. A 90/10 splitter is used to couple 90% and 10% of the light to an Anritsu MS9740A OSA and Tektronix DSA 8300 sampling oscilloscope with built-in photodiode, respectively. The OSA monitoring allows to appropriately tune the bandpass filter whereas the time-dependent power levels in the two wavelength channels are monitored with the oscilloscope. As proof-of-principle wavelength tuning is done by periodically switching the bias between Gate 1 and Gate 2 and between Gate 3

Optics EXPRESS

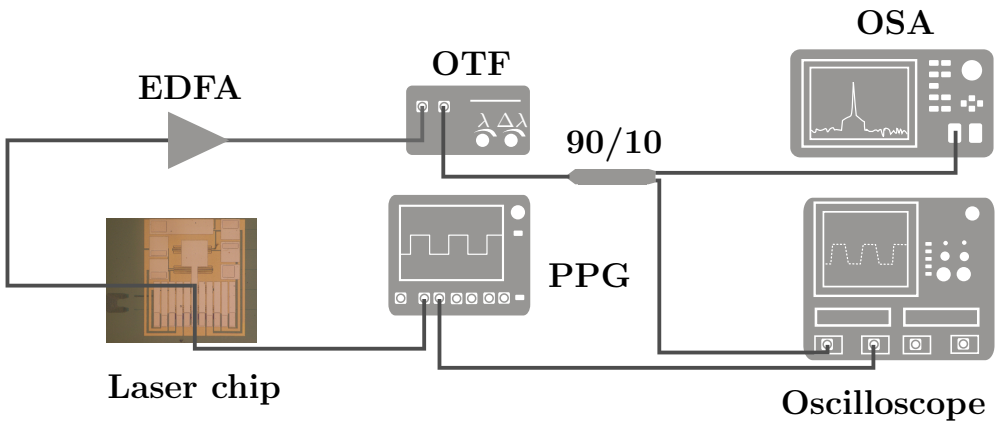

Fig. 9. Schematic of the optical setup to measure the wavelength switching characteristics.

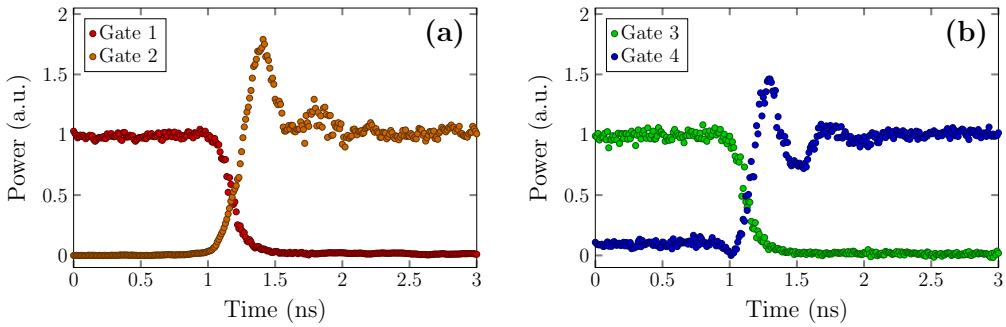

Fig. 10. Wavelength switching characteristics. (a) Switching from Gate 1 to Gate 2; (b) Switching from Gate 3 to Gate 4.

and Gate 4 with a 500 ns periodic rectangular 0.75 V (~ 0 mA) – 1.1 V (50 mA) pulse train. Similar switching behavior can be expected between non-neighboring wavelength channels. The wavelength switching characteristics are shown in Fig. 10(a) and 10(b), for switching from Gate 1 to Gate 2 and from Gate 3 to Gate 4, respectively. Clearly, wavelength switching occurs in less than a nanosecond with a rise time of 195 ps and 135 ps, respectively. The fall time is 190 ps and 185 ps, respectively. Hereby rise (fall) time is defined as the time it takes for the response to rise (fall) from 10% (90%) to 90% (10%) of the steady-state response.

5. Conclusion

We have demonstrated fast wavelength switching with a four-channel InP-on-silicon laser that exploits filtered feedback to achieve single-mode laser operation and tunability. At room temperature the laser has a threshold current of 20 mA with a maximum waveguide-coupled output power of 4 mW. CW operation up to 65°C is achieved. Wavelength switching times are less than 1 ns and each wavelength channel can be directly modulated at 12.5 Gbit/s, making the structure very useful for optical packet or burst switching applications.

Funding

The authors acknowledge the Methusalem programme of the Flemish government for funding.

Optics EXPRESS

Acknowledgments

The authors acknowledge L. Van Landschoot for the SEM images, S. Verstuyft and M. Muneeb for support with metallization and A. Abbasi for help with high-speed characterization.